Probing the Metal-Insulator Transition in BaTiO_{3} by Electrostatic Doping

Santosh Raghavan, Jack Y. Zhang, Omor F. Shoron, and Susanne Stemmer

Phys. Rev. Lett. **117**, 037602 — Published 14 July 2016

DOI: 10.1103/PhysRevLett.117.037602

Probing the metal-insulator transition in $BaTiO_3$ by electrostatic doping

Santosh Raghavan, Jack Y. Zhang, Omor F. Shoron, and Susanne Stemmer[a)]

Materials Department, University of California, Santa Barbara, California, 93106-5050, USA.

[a)] Corresponding author. Email: stemmer@mrl.ucsb.edu

Abstract

The metal-to-insulator transition in $BaTiO_3$ is investigated using electrostatic doping, which avoids effects from disorder and strain that would accompany chemical doping. $SmTiO_3/BaTiO_3/SrTiO_3$ heterostructures are doped with a constant sheet carrier density of 3×10^{14} cm^{-2} that is introduced via the polar $SmTiO_3/BaTiO_3$ interface. Below a critical $BaTiO_3$ thickness, the structures exhibit metallic behavior with high carrier mobilities at low temperatures, similar to $SmTiO_3/SrTiO_3$ interfaces. Above this thickness, data indicate that the $BaTiO_3$ layer becomes ferroelectric. The $BaTiO_3$ lattice parameters increase to a value consistent with a strained, tetragonal unit cell, the structures are insulating below ~ 125 K, and the mobility drops by more than an order of magnitude, indicating self-trapping of carriers. The results shed light on the interplay between charge carriers and ferroelectricity.

The coexistence of ferroelectric and metallic behavior has been a subject of fundamental interest since at least the 1960s [1-5]. Modern understanding of ferroelectric materials such as $BaTiO_3$ shows that they rely on an unstable transverse optical (TO) phonon mode *and* large splitting of the TO and longitudinal optical (LO) modes [6]. Free carriers screen the long range Coulomb interactions that give rise to the LO-TO splitting [7] and thus are expected to destabilize ferroelectricity [6, 8]. An important question, which is also relevant for practical applications, is therefore what happens when charge carriers are introduced into a ferroelectric, for example by doping. In $BaTiO_3$, which is a prototypical ferroelectric, some studies indicate that ferroelectricity and metallic behavior may co-exist [3, 9], while others have suggested that they only do so in separated regions [10]. A related observation is that doped ferroelectric single crystals and ceramics require very high doping levels to induce an insulator-to-metal transition [11-13]. This appears to be consistent with the picture that ferroelectricity and metallicity cannot easily coexist. The nature of the doped ferroelectric is crucial for understanding how free carriers and ferroelectric polarization interact. For example, prior studies use chemically doped samples, which induces large amounts of disorder. Thus, not surprisingly, disorder has been invoked as an important factor in promoting the insulating state [12, 13]. Furthermore, large concentrations of dopant atoms may also introduce lattice distortions that may contribute to destabilizing ferroelectricity. Improved understanding could be obtained if carriers could be introduced in a ferroelectric without chemical doping, thereby avoiding the structural distortion and disorder effects associated with foreign atoms.

Oxide heterostructures allow for introducing charge carriers by purely electrostatic means [14, 15]. For example, the polar discontinuity at interfaces between the insulators $R\mathrm{TiO}_3$ (R is a trivalent rare earth ion, such as Sm or Gd) and $SrTiO_3$ has been used to electrostatically

introduce large sheet carrier densities (~3×10^{14} cm^{-2}) into $SrTiO_3$ [16, 17] to study (Mott) MITs [18-23]. In such two-dimensional electron liquids (2DELs) a substantial portion of the carriers is confined near the interface, in addition to more weakly confined electrons that spread into the $SrTiO_3$ [24-28]. The conduction band alignments [29] prevent carriers from spreading into the $RTiO_3$ [16]. Here, we use the polar $SmTiO_3/BaTiO_3$ interface to introduce charge carriers into $SmTiO_3/BaTiO_3/SrTiO_3$ heterostructures, as shown in schematically in Fig. 1(a). $BaTiO_3$ films of increasing thickness are inserted into the $SmTiO_3/SrTiO_3$ interface. For *paraelectric* $BaTiO_3$ the carrier density and distribution are expected to be similar to structures without $BaTiO_3$, due to similar fixed polar charges, material properties, and band offsets, see Fig. 1(b). We show that above a critical $BaTiO_3$ thickness, corresponding to ~ two unit cells (u.c.s), structure and transport properties abruptly change, consistent with the appearance of ferroelectricity in the $BaTiO_3$. We discuss the carrier transport in this regime and show that it provides insights into the interaction between mobile carriers and ferroelectricity and the nature of the insulating state.

Layers were grown by hybrid molecular beam epitaxy (MBE) on (001) $(LaAlO_3)_{0.3}(Sr_2AlTaO_6)_{0.7}$ (LSAT), as described elsewhere [30, 31], and are coherently strained to the LSAT substrate (lattice parameter: 0.386 nm). The thickness of the $SmTiO_3$ and $SrTiO_3$ layers is kept constant at 5 nm and 20 nm respectively, and the $BaTiO_3$ thickness is varied between ½ and 13 u.c.s. In the following, we specify the $BaTiO_3$ thickness by the number of BaO planes it contains, see Fig. 1(a). Oscillations in the intensity of in-situ reflection high-energy electron diffraction (RHEED) patterns [32] of all layers indicated layer-by-layer growth and allowed for precise thickness control during growth. On-axis x-ray diffraction (XRD) showed only film and substrate reflections [Fig. 1(b)]. XRD, oscillations in RHEED intensity, and high-angle annular dark-field scanning transmission electron microscopy (HAADF-STEM)

were used to confirm the thicknesses and structural quality of the heterostructures. All samples exhibit Laue thickness fringes in XRD indicating smooth interfaces and high quality epitaxy. The 20 nm $SrTiO_3$ films give rise to closely spaced Laue fringes seen in all samples in Fig. 1(b) and widely spaced fringes from the 5 nm $SmTiO_3$ layer are visible. For larger $BaTiO_3$ thicknesses, the peaks from the $BaTiO_3$ interfere and the interference pattern becomes more complex.

For electrical characterization (resistivity and Hall measurements) in a Physical Property Measurement System (Quantum Design PPMS Dynacool), 50 nm Ti/400 nm Au Ohmic contacts were deposited in Van der Pauw geometry on the $SmTiO_3$ layer. The Hall voltage as a function of magnetic field was linear up to ±9 T, similar to $RTiO_3/SrTiO_3$ interfaces [16, 35]. Ferroelectricity hysteresis loops of $BaTiO_3$ films were measured by piezo-force microscopy (PFM) and capacitance-voltage (C-V) measurements [32]. For HAADF-STEM, cross section samples were prepared by focused ion beam thinning and imaged on an FEI Titan S/TEM operated at 300 kV with 9.6 mrad convergence angle. The images shown here consisted of 100 fast-scan images, which were acquired with a 3 μs dwell time and 512 × 512 pixels, and averaged using sub-pixel cross correlation to reduce the effect of drift and scan distortions.

All samples exhibited Hall sheet carrier densities (n_{2D}) at 300 K of ~ 3×10^{14} cm^{-2} [Fig. 2(a)], independent of the $BaTiO_3$ thickness. Thus, a 2DEL forms at the $SmTiO_3/BaTiO_3$ interface, with n_{2D} corresponding to the value that compensates the fixed polar charge at the interface. Aside from a small decrease for thicker films, n_{2D} is almost independent of the temperature (T). The T-dependence of the sheet resistance R_s [Fig. 2(b)] for samples with $BaTiO_3$ thicknesses between 1 to 3 BaO layers shows metallic behavior (defined as $\delta R_S/\delta T > 0$), except for a slight upturn at low temperatures that could be weak localization. A pronounced

increase in R_s occurs for samples with more than 4 BaO layers and $\delta R_S/\delta T < 0$ below 125 K. The Hall mobility, μ, for samples with $BaTiO_3$ thicknesses below 4 BaO layers is similar to that of RTiO$_3$/SrTiO$_3$ interfaces Fig. 2(c)] [36]. At low T, μ of RTiO$_3$/SrTiO$_3$ interfaces is dominated by interface roughness scattering, while at higher T it is limited by electron-electron scattering ($\mu^{-1} \sim T^2$) 36]. SmTiO$_3$/BaTiO$_3$/SrTiO$_3$ heterostructures show similar transport characteristics, *but only for BaTiO$_3$ thicknesses less than 4 BaO layers*. This can be seen from the fits in Fig. 2(c), which show that the data is described as $\mu^{-1} = \mu_0^{-1} + \alpha T^2$, where μ_0 is the disorder (defects, interface roughness, etc.) limited mobility and α is the strength of electron-electron scattering, which had values similar to that of the RTiO$_3$/SrTiO$_3$ interfaces ($1.2 - 1.9\times10^{-6}$ Vscm^{-2}K^{-2}). The absence of LO phonon mode scattering, which limits the mobility of bulk doped SrTiO$_3$ at room temperature, indicates screening by the large density of free carriers [36]. To describe the data of the sample with 4 BaO layers, LO phonon scattering is included to obtain a fit of comparable quality (see Fig. 2), i.e., $\mu^{-1} = \mu_0^{-1} + \alpha T^2 + \mu_{LO}^{-1}$, where μ_{LO} is the LO phonon scattering limited mobility. It is given as $\mu_{LO} = \frac{K_{LO}}{\hbar\omega_{LO}}\left(\exp\left(\frac{\hbar\omega_{LO}}{k_B T}\right) - 1\right)$, where $\hbar$ is the reduced Planck's constant, k_B the Boltzmann constant, $\hbar\omega_{LO}$ the (effective) energy of the LO phonon(s), and K_{LO} is given in ref. [37]. Furthermore, the 4 BaO layer sample shows a large decrease in μ_0 by a factor of five. For thicknesses greater than 4 BaO layers, the mobility drops further, to below 10 cm^{2}V^{-1}s^{-1}. For these samples, the low-temperature mobility increases initially with temperature, then decreases with further increase in temperature. No attempt was made to fit the mobility data for the samples with > 4 BaO layers.

Figure 3(a) shows HAADF-STEM cross-section images of samples with nominally 8 BaO layers (left) and 3 BaO layers (right), respectively. Thickness variations of ±1 monolayer

are associated with steps. The average number of BaO layers over the entire TEM sample matches the thickness calibrated using RHEED oscillations. Abrupt $SrTiO_3$/$BaTiO_3$ interfaces with clear atomic number (*Z*)-contrast can be seen. The $BaTiO_3$/$SmTiO_3$ interface has a smaller *Z*-difference, and is located using the A-site cation off-centering in the $SmTiO_3$, not present in $BaTiO_3$ [19]. Figure 3(b) shows a map of the relative out-of-plane and in-plane lattice parameters of the $SrTiO_3$ and $BaTiO_3$ layers measured from Fig. 3(a), normalized to the $SrTiO_3$. The in-plane values are ~1.00, consistent with coherently strained films. The out-of-plane values are all > 1.00 in the $BaTiO_3$. The 8 BaO sample shows a relative out-of-plane value of ~ 1.057 in the interior, which matches the theoretically expected value for compressively strained, c-axis-oriented, tetragonal $BaTiO_3$ [dashed lines in Fig. 3(c)]. The out-of-plane values are reduced near the interfaces and remain completely below the theoretically predicted value in the 3 BaO layer film, indicating reduced tetragonality.

We next discuss the origins of the different transport characteristics of samples with < and > 4 BaO layers, respectively. We note that all $BaTiO_3$ films, independent of their thickness, were electrostatically doped due to the polar discontinuity with $SmTiO_3$. Samples show metallic behavior and carrier mobilities consistent with band conduction only when the $BaTiO_3$ is extremely thin (≤ 2 u.c.s). Such thin layers are characterized by reduced tetragonality and the absence of LO phonon scattering at high temperature, indicating that these layers are not ferroelectric. "Deadlayers" of a few u.c.s are common for ferroelectric films [38, 39]. The HAADF-STEM images show that they are correlated with a reduced tetragonality of the unstrained unit cell. The transport characteristics of samples with thin $BaTiO_3$, including the mobilities and the temperature dependence are comparable to *R*TiO_3/$SrTiO_3$ samples [16, 36],

indicating that 2DELs at interfaces with *paraelectric* $BaTiO_3$ do not have fundamentally different properties.

Thicker $BaTiO_3$ films (> 4 BaO layers) show increased lattice distortion, consistent with a tetragonal unstrained unit cell and a ferroelectric film. Although measurement of polarization switching, which is the only definitive proof for ferroelectricity, is not possible for such conductive layers, the results nevertheless suggest the microscopic conditions for ferroelectricity exist (tetragonal distortion, LO phonon scattering in the 4 BaO sample). Hysteresis in PFM and C-V measurements of similar structures indicate ferroelectricity in $BaTiO_3$ layers of comparable thickness and grown by the same method [32]. Furthermore, the transport characteristics of structures with thicker $BaTiO_3$ films (> 4 BaO layers) imply that the carriers cease to spread into the $SrTiO_3$, as in this case transport would show high-mobility, metallic characteristics. This can be explained with the presence of the internal ferroelectric polarization field, which causes a change in the spatial distribution of the charge carriers compared to a structure with paraelectric $BaTiO_3$. Specifically, the calculations in Fig. 1(c) show that carriers are located only within the $BaTiO_3$ layer when a ferroelectric polarization is present. The decrease in μ_0 of the 4 BaO layer sample can thus be explained with the redistribution of the portion of the 2DEL that was located far in the $SrTiO_3$ closer to the $SmTiO_3/BaTiO_3$ interface (where the carriers suffer from interface roughness scattering).

The very low mobilities (1-10 $cm^2V^{-1}s^{-1}$) of carriers in ferroelectric samples with > 4 BaO layers are consistent with self-trapping of carriers (also known as strong coupling polarons [40]). In particular, at low temperatures, the mobility increases initially as the temperature is raised. This cannot be described by a temperature-independent disorder term μ_0. Furthermore, the samples show insulating characteristics in this regime, despite the fact that the sheet resistances

remain below the Mott-Ioffe-Regel limit, of ~ 10 kΩ/□, where strong localization must occur [41]. The low mobilities are similar to those of single crystal, doped $BaTiO_3$ [42]; thus the very sluggish conduction, typical of polarons, appears to be a general feature of carriers in ferroelectric $BaTiO_3$, independent of how the carriers are introduced, i.e. chemical vs. electrostatic doping, i.e. the degree and type of disorder. The temperature dependence of the transport characteristics of self-trapped carriers can be complicated [43] and standard models for transport of strong-coupling polarons often fail for real materials [44].

The results thus show that the appearance of ferroelectricity coincides with the transition from a high-mobility, metallic state to a low-mobility, high-resistance state, with insulating characteristics at low temperature. As the sheet carrier density and other parameters are kept constant, this transition reflects the intrinsic interactions between (free, mobile) charge carriers and the ferroelectric polarization. The ferroelectric film does not tolerate mobile free carriers: carriers are pushed out of the interior towards the interface, where they conduct with low mobility and the temperature-dependence is consistent with self-trapping. The MIT is thus reminiscent of a Mott-type transition, in the sense that it occurs when the long-range Coulomb forces are insufficiently screened. With regards to the question as to whether ferroelectricity and mobile carriers can co-exist, the answer appears to be yes, but not with conventional, metallic conduction within the bulk of the ferroelectric. Finally, the method of electrostatic doping may be useful in the future for example in understanding other intrinsic aspects of polarons for which a quantitative understanding is often missing.

Acknowledgements

The authors gratefully acknowledge very useful discussions with David Emin and Boris Shklovskii. This work was supported in part by the MRSEC Program of the NSF under Award No. DMR 1121053, which also supported the MRL Shared Experimental Facilities used in this work, and in part by the Center for Low Energy Systems Technology (LEAST), one of six centers of STARnet, a Semiconductor Research Corporation program sponsored by MARCO and DARPA. The microscopy work was supported by the DOE (DEFG02-02ER45994).

References

[1] P. W. Anderson, and E. I. Blount, Phys. Rev. Lett. **14**, 217 (1965).

[2] E. F. Steigmeier, and G. Harbeke, Solid State Comm. **8**, 1275 (1970).

[3] Y. Wang, X. H. Liu, J. D. Burton, S. S. Jaswal, and E. Y. Tsymbal, Phys. Rev. Lett. **109**, 247601 (2012).

[4] D. Puggioni, and J. M. Rondinelli, Nat. Comm. **5**, 3432 (2014).

[5] Y. G. Shi, Y. F. Guo, X. Wang, A. J. Princep, D. Khalyavin, P. Manuel, Y. Michiue, A. Sato, K. Tsuda, S. Yu, M. Arai, Y. Shirako, M. Akaogi, N. L. Wang, K. Yamaura, and A. T. Boothroyd, Nat. Mater. **12**, 1024 (2013).

[6] W. Zhong, R. D. King-Smith, and D. Vanderbilt, Phys. Rev. Lett. **72**, 3618 (1994).

[7] A. Mooradia, and G. B. Wright, Phys. Rev. Lett. **16**, 999 (1966).

[8] Y. Iwazaki, T. Suzuki, Y. Mizuno, and S. Tsuneyuki, Phys. Rev. B **86**, 214103 (2012).

[9] T. Kolodiazhnyi, M. Tachibana, H. Kawaji, J. Hwang, and E. Takayama-Muromachi, Phys. Rev. Lett. **104**, 147602 (2010).

[10] I.-K. Jeong, S. Lee, S.-Y. Jeong, C. J. Won, N. Hur, and A. Llobet, Phys. Rev. B **84**, 064125 (2011).

[11] T. Kolodiazhnyi, Phys. Rev. B **78**, 045107 (2008).

[12] K. Page, T. Kolodiazhnyi, T. Proffen, A. K. Cheetham, and R. Seshadri, Phys. Rev. Lett. **101**, 205502 (2008).

[13] J. A. Bock, S. Lee, S. Trolier-McKinstry, and C. A. Randall, Appl. Phys. Lett. **107**, 092902 (2015).

[14] C. H. Ahn, A. Bhattacharya, M. Di Ventra, J. N. Eckstein, C. D. Frisbie, M. E. Gershenson, A. M. Goldman, I. H. Inoue, J. Mannhart, A. J. Millis, A. F. Morpurgo, D. Natelson, and J. M. Triscone, Rev. Mod. Phys. **78**, 1185 (2006).

[15] S. Stemmer, and S. J. Allen, in *Ann. Rev. Mater. Res.*, edited by D. R. Clarke (Annual Reviews, Palo Alto, 2014), pp. 151.

[16] P. Moetakef, T. A. Cain, D. G. Ouellette, J. Y. Zhang, D. O. Klenov, A. Janotti, C. G. Van de Walle, S. Rajan, S. J. Allen, and S. Stemmer, Appl. Phys. Lett. **99**, 232116 (2011).

[17] J. S. Kim, S. S. A. Seo, M. F. Chisholm, R. K. Kremer, H. U. Habermeier, B. Keimer, and H. N. Lee, Phys. Rev. B **82**, 201407 (2010).

[18] P. Moetakef, C. A. Jackson, J. Hwang, L. Balents, S. J. Allen, and S. Stemmer, Phys. Rev. B. **86**, 201102(R) (2012).

[19] J. Y. Zhang, J. Hwang, S. Raghavan, and S. Stemmer, Phys. Rev. Lett. **110**, 256401 (2013).

[20] R. Chen, S. Lee, and L. Balents, Phys. Rev. B **87**, 161119(R) (2013).

[21] F. Lechermann, and M. Obermeyer, New J. Phys. **17**, 043026 (2015).

[22] R. Pentcheva, and W. E. Pickett, Phys. Rev. Lett. **99**, 016802 (2007).

[23] L. Bjaalie, A. Janotti, B. Himmetoglu, and C. G. Van de Walle, Phys. Rev. B **90**, 195117 (2014).

[24] W. J. Son, E. Cho, B. Lee, J. Lee, and S. Han, Phys. Rev. B **79**, 245411 (2009).

[25] M. Stengel, Phys. Rev. Lett. **106**, 136803 (2011).

[26] P. Delugas, A. Filippetti, V. Fiorentini, D. I. Bilc, D. Fontaine, and P. Ghosez, Phys. Rev. Lett. **106**, 166807 (2011).

[27] G. Khalsa, and A. H. MacDonald, Phys. Rev. B **86**, 125121 (2012).

[28] S. Y. Park, and A. J. Millis, Phys. Rev. B **87**, 205145 (2013).

[29] L. Bjaalie, B. Himmetoglu, L. Weston, A. Janotti, and C. G. Van de Walle, New J. Phys. **16**, 025005 (2014).

[30] B. Jalan, R. Engel-Herbert, N. J. Wright, and S. Stemmer, J. Vac. Sci. Technol. A **27**, 461 (2009).

[31] P. Moetakef, J. Y. Zhang, S. Raghavan, A. P. Kajdos, and S. Stemmer, J. Vac. Sci. Technol. A **31**, 041503 (2013).

[32] See supplementary information [URL to be inserted by publisher], which contains refs. [33,34], for details for the materials parameters used in the band profile calculations, reflection high-energy electron-diffraction (RHEED) data acquired during MBE growth, and piezoforce microscopy and CV measurements of $BaTiO_3$ films grown by MBE.

[33] M. Cardona, Phys. Rev. **140**, A651 (1965).

[34] L. Bjaalie, A. Verma, B. Himmetoglu, A. Janotti, S. Raghavan, V. Protasenko, E. H. Steenbergen, D. Jena, S. Stemmer, and C. G. Van de Walle, Phys. Rev. B **92**, 085111 (2015).

[35] C. A. Jackson, J. Y. Zhang, C. R. Freeze, and S. Stemmer, Nat. Commun. **5**, 4258 (2014).

[36] E. Mikheev, B. Himmetoglu, A. P. Kajdos, P. Moetakef, T. A. Cain, C. G. Van de Walle, and S. Stemmer, Appl. Phys. Lett. **106**, 062102 (2015).

[37] A. Verma, A. P. Kajdos, T. A. Cain, S. Stemmer, and D. Jena, Phys. Rev. Lett. **112**, 216601 (2014).

[38] Y. S. Kim, D. H. Kim, J. D. Kim, Y. J. Chang, T. W. Noh, J. H. Kong, K. Char, Y. D. Park, S. D. Bu, J.-G. Yoon, and J.-S. Chung, Appl. Phys. Lett. **86**, 102907 (2005).

[39] D. D. Fong, G. B. Stephenson, S. K. Streiffer, J. A. Eastman, O. Auciello, P. H. Fuoss, and C. Thompson, Science **304**, 1650 (2004).

[40] D. Emin, *Polarons* (Cambridge University Press, Cambridge, 2013).

[41] N. F. Mott, Philos. Mag. **26**, 1015 (1972).

[42] T. Kolodiazhnyi, A. Petric, M. Niewczas, C. Bridges, A. Safa-Sefat, and J. E. Greedan, Phys. Rev. B **68**, 085205 (2003).

[43] D. Emin, Adv. Physics **22**, 57 (1973).

[44] S. Fratini, and S. Ciuchi, Phys. Rev. Lett. **91**, 256403 (2003).

[45] G. Snider, *1D Poisson Freeware (*http://www3.nd.edu/~gsnider/).

Figure Captions

Figure 1. (a) Schematic of the heterostructure. The thickness of the $BaTiO_3$ layer is specified in terms of the number of BaO layers it contains. The grey-shaded area indicates the 2DEL, which spreads into the $BaTiO_3/SrTiO_3$ layers. (b,c) Calculated conduction band profiles and 2DEL charge distributions for the $SmTiO_3/BaTiO_3/SrTiO_3$ heterostructures, with (b) two u.c.s of a paraelectric $BaTiO_3$ layer (c) seven u.c.s of a ferroelectric $BaTiO_3$ layer. The calculations were performed with a one-dimensional Poisson-Schrödinger solver [45], using the parameters described in the Supplementary Information [32]. (d) On-axis XRD patterns of the 5-nm-$SmTiO_3$/*x*-BaO ($BaTiO_3$)/20-nm-$SrTiO_3$/LSAT heterostructures. The dashed lines indicate the expected peak positions for individual layers coherently strained to a LSAT substrate.

Figure 2. (a) Sheet carrier density, n_{2D}, (b) sheet resistance R_s, and (c) mobility μ as a function of temperature T, for $SmTiO_3/BaTiO_3/SrTiO_3$/(001)LSAT samples with different $BaTiO_3$ thicknesses (specified in number of BaO layers). The dashed lines are guides to the eye and the solid lines in (c) are fits to the data. For the three thinnest $BaTiO_3$ structures, fits of form $\mu^{-1} = \mu_0^{-1} + \alpha T^2$ were used and resulted in (goodness of fit) chi-squared values of less than 0.006. Such fits yielded an increased chi-squared value for the 4 BaO sample (0.01). Including LO-phonon scattering ($\mu^{-1} = \mu_0^{-1} + \alpha T^2 + \mu_{LO}^{-1}$) reduced the chi-squared value to 0.003 and the average energy of the LO phonon obtained from the fit is 50 meV. The drop in the mobility at low temperatures for this sample is due to the low μ_0.

Figure 3. (a) HAADF STEM cross-sections of 8 BaO (left) and 3 BaO (right) thick layers of $BaTiO_3$. The $SrTiO_3$ and $SmTiO_3$ layers are to the left and right of the $BaTiO_3$, respectively.

The arrows mark the approximate interface boundaries. (b) Maps of unit cell lattice parameters along the out-of-plane and in-plane directions, normalized to the lattice parameter of the 3 layers of $SrTiO_3$ farthest away from the $BaTiO_3$. Only $SrTiO_3$ and $BaTiO_3$ layers are mapped. (c) Averaged (parallel to the interface) in-plane (orange circle) and out-of-plane (blue square) lattice parameters from (b). The dashed lines indicate the theoretically expected value for compressively strained, c-axis oriented, tetragonal $BaTiO_3$ on a LSAT substrate.

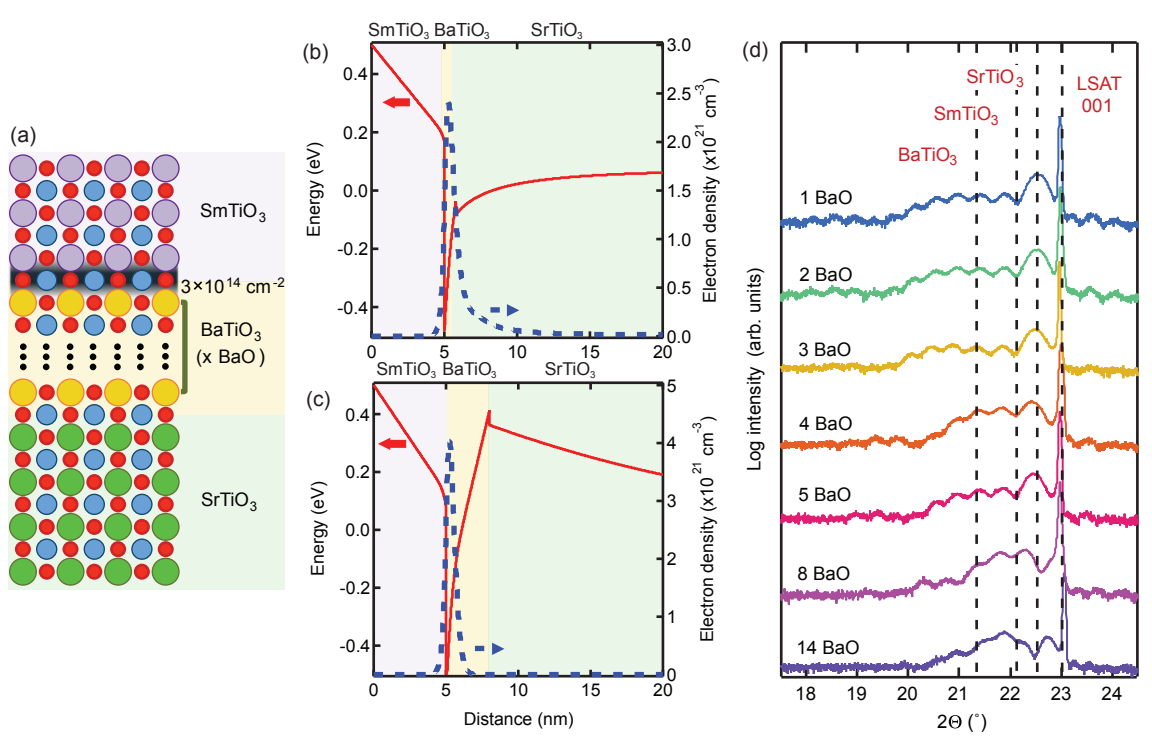
(a)
SmTiO3
3×10^14 cm^-2
BaTiO3
(x BaO)
SrTiO3
(b)
SmTiO3 BaTiO3 SrTiO3
Energy (eV)
Electron density (x10^21 cm^-3)
(c)
SmTiO3 BaTiO3 SrTiO3
Energy (eV)
Electron density (x10^21 cm^-3)
Distance (nm)
(d)
SrTiO3
SmTiO3
BaTiO3
LSAT
001
1 BaO
2 BaO
3 BaO
4 BaO
5 BaO
8 BaO
14 BaO
Log intensity (arb. units)
2Θ (°)

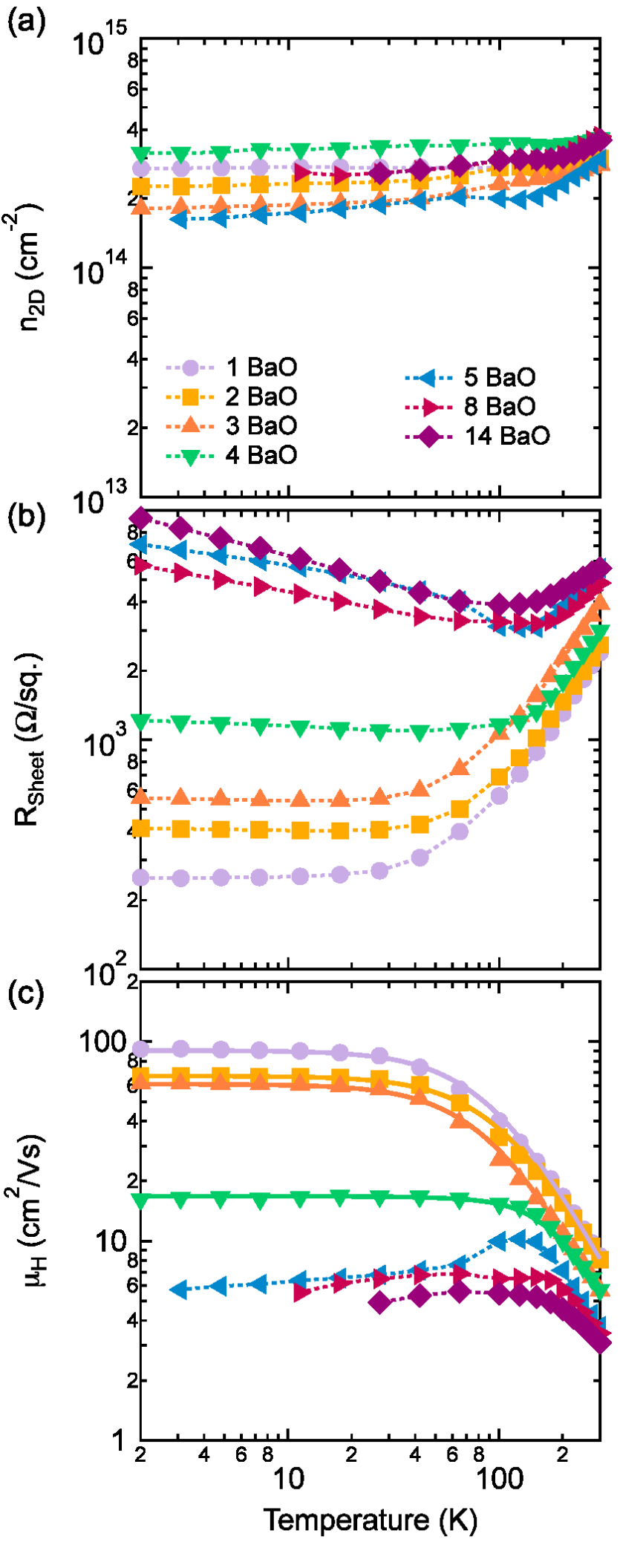
(a)
10^{15}
10^{14}
10^{13}
n_{2D} (cm^{-2})
1 BaO
2 BaO
3 BaO
4 BaO
5 BaO
8 BaO
14 BaO
(b)
10^{3}
10^{2}
R_{Sheet} (Ω/sq.)
(c)
100
10
1
μ_H (cm^2/Vs)
2
4
6
8
10
100
Temperature (K)

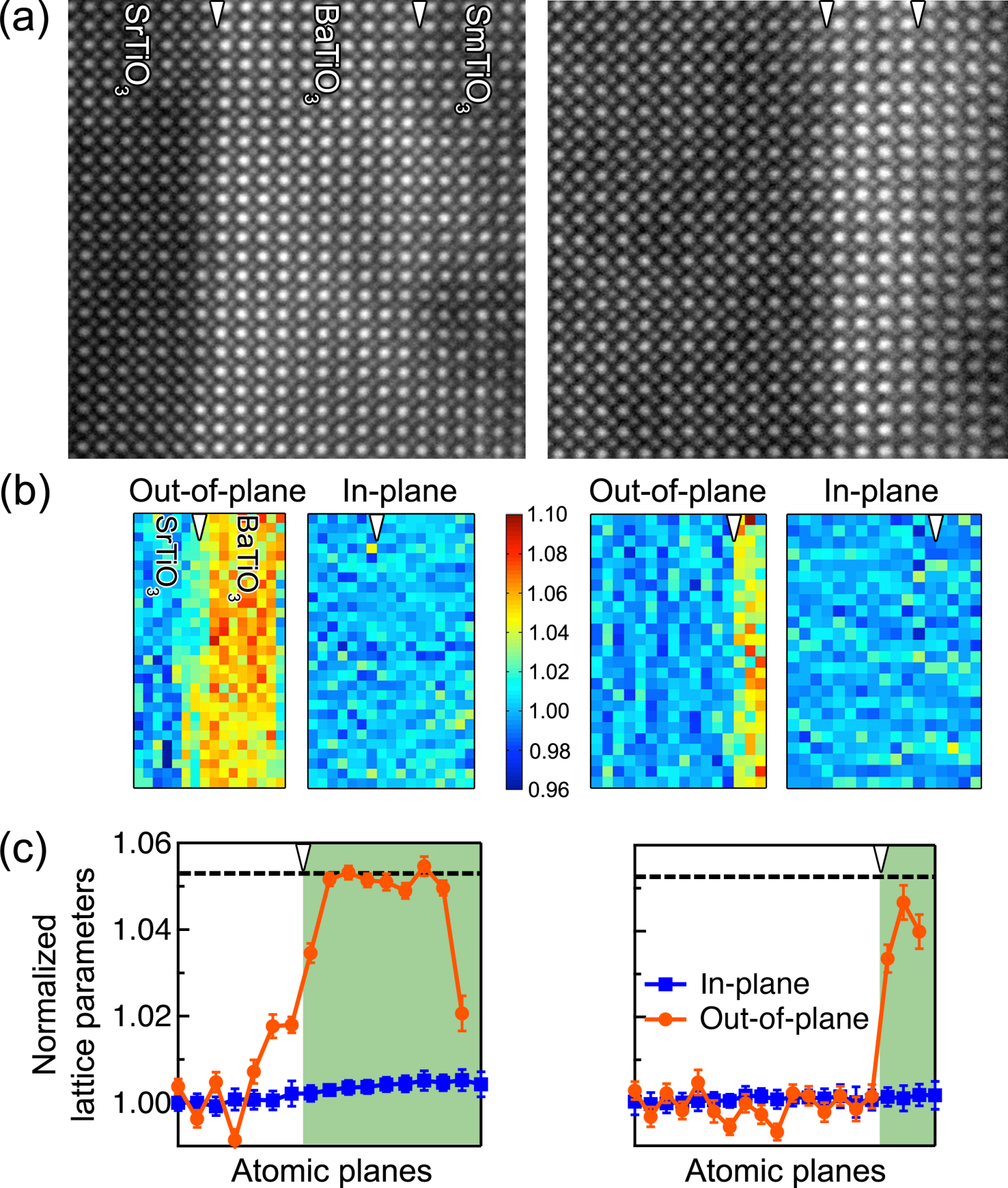
(a)
SrTiO3
BaTiO3
SmTiO3
(b)
Out-of-plane
In-plane
Out-of-plane
In-plane
SrTiO3
BaTiO3
1.10
1.08
1.06
1.04
1.02
1.00
0.98
0.96
(c)
Normalized lattice parameters
1.06
1.04
1.02
1.00
Atomic planes
In-plane
Out-of-plane
Atomic planes